Scientia Iranica B (2014) 21(2), 370–386

SCIENTIA IRANICA

Sharif University of Technology
Scientia Iranica
Transactions B: Mechanical Engineering
www.scientiairanica.com

Investigation of unsteady parameter effects on aerodynamic coefficients of pitching airfoil using coarse grid simulation

A. Heydari[a,*], Ma. Pasandideh-Fard[a] and M. Malekjafarian[b]

a. *Department of Mechanical Engineering, Faculty of Engineering, Ferdowsi University of Mashhad, Mashhad, P.O. Box 91775-1111I, Iran.*
b. *Department of Mechanical Engineering, Faculty of Engineering, University of Birjand, Birjand, Iran.*

Received 1 September 2012; received in revised form 10 July 2013; accepted 21 September 2013

KEYWORDS
Pitching airfoil;
Coarse grid CFD;
Surface vorticity confinement;
Multi zone adaptive spring network.

Abstract. In this article, the effects of unsteady parameters, including mean angle of attack, oscillation amplitude, reduced frequency, and pitching axis position, on the aerodynamic coefficients of a pitching airfoil are studied. This investigation is implemented for high Reynolds number flows around a dynamic stall condition. The employed numerical method is a Coarse Grid CFD (CGCFD) method, in which the Euler equations are solved using a coarse grid with no slip boundary conditions, and a compressible surface vorticity confinement technique. The required computational time for this method is significantly lower compared to that of the full Navier-Stokes equations with a simple one-equation turbulence model. In addition, a multi zone adaptive spring grid network is applied to simulate the moving boundary, which further reduces the computational time. Using the described numerical setup separates the current work from the others. The obtained numerical predictions are in very good agreement with experimental data for the high Reynolds number flow. It is found that moving the pitching axis position to the right or left outside, and distancing it from the trailing edge or leading edge, has an inverse effect on aerodynamic characteristics. Furthermore, increasing reduced frequency results in a reduction in the lift hysteresis loop slope, and in the maximum lift and drag coefficients.

1. Introduction

In the past two decades, research into flapping airfoils suitable for Micro Air Vehicles (MAVs) and rotors dynamics has increased continuously. Rotary-wing aircraft frequently work in very complex aerodynamic situations that limit their performance, creating an extended range of difficult problems for engineers. The most serious problems to be considered are those related to the main rotor system with pitching motion, which include shear layers, vortices around body surfaces and vortex dominated regions behind the bodies. At very high speeds and in maneuvering flights, a rotor can experience the effects of transonic flow, flow reversal, and dynamic stall, due to the strong induced flow effects and interaction with the wake in the custom operation. Unsteady studies are extremely useful in understanding flow characteristics and estimating the dependence of the aerodynamic performance on different parameters, such as the amplitude of oscillation, reduced frequency, pitching axis position, Re, and kinematic patterns. For the same angle of attack, the airfoil produces higher lift and drag forces during the down-

*. *Corresponding author. Tel./Fax: +98 511 8763304*
E-mail addresses: heydary.a@gmail.com (M. Heydari); Fard_m@um.ac.ir (M. Pasandideh-Fard); mmjafarian@excite.com (M. Malekjafarian)

stroke phase than during the up-stroke. The generation of hysteresis loops is the result of induced velocities, which lead to different lift and drag coefficients between up-stroke and down-stroke.

In the first investigations, McCroskey [1] and Piziali [2] expressed a perfect experimental review of pitching airfoils. Tuncer et al. [3] investigated a numerical model for the unsteady flow around airfoils that pitch sinusoidally, associating this with the dynamic stall phenomenon. They have also added the algebraic Baldwin-Lomax turbulence model. The airfoils pitch between (5°-25°), at reduced frequencies equal to 0.2, 0.3 and 0.5, at a Reynolds number (Re) of 1×10^6. The growth and movement of the leading edge vortex have been investigated in detail with a fully viscous flow analysis and high required computational time. Numerical observations have been compared with experiments and good agreement has been reported. Akbari and Price [4] solved incompressible Navier-Stokes equations to simulate flows around a pitching airfoil with high oscillation amplitudes. A laminar flow has been modeled at Reynolds number, $\mathrm{Re} = 1 \times 10^4$. They checked the effects of parameters, including reduced frequency, Reynolds number and mean angle of attack. The pitching angles have been changed around the static stall angle of attack 15°, and the reduced frequencies were set at 0.3, 0.5 and 1. Results under these conditions have been compared with Tuncer's observations [3].

Recently, investigations into unsteady parameter effects in pitching motion have been extended. Sarkar and Venkatraman [5] studied the dynamic stall of a symmetric airfoil at medium to high reduced frequencies (beyond 1), as maximum angle of attack varies from 25° to 45°. They modeled the fluid flow field using a discrete vortex technique. The effect of reduced frequencies on the vortex structure and the aerodynamic load coefficients is evaluated. They detected a periodic doubling pattern in the vortex behavior at higher frequency range, which has not previously been reported. Martinat et al. [6] provided 2-D and 3-D numerical simulations of the NACA0012 dynamic stall at Reynolds numbers 105 and 106 using various turbulence models. The turbulent effect on the hysteresis curve of aerodynamic coefficients was studied by statistical modeling. The turbulence modeling performance was checked by comparing classical and advanced URANS approaches. Also, it has been indicated that the down-stroke phases of pitching motion are faced with strong three-dimensional turbulence effects along the span, whereas the flow can be assumed practically two-dimensional during the upward motion. Amiralaei et al. [7] studied the LRN aerodynamics of a harmonically pitching NACA0012 airfoil. In their work, the influence of unsteady parameters, namely, oscillation amplitude, reduced frequency, and Reynolds number, on the aerodynamic performance of the model, is investigated. This study is conducted to investigate the effect of Re number in the range $555 < \mathrm{Re} < 5000$, oscillation amplitude between 2° and 10°, and reduced frequency in the range of $0.1 < k < 0.25$. The simulation was performed in an OpenFOAM simulator. You and Bromby [8] performed a Large-Eddy Simulation (LES) of turbulent flow over a pitching airfoil at realistic Reynolds and Mach numbers. They employed an unstructured-grid LES technology and a hybrid implicit-explicit time-integration scheme to provide a highly efficient way for treating time-step size restriction in the separated flow region. It indicated that characteristics of flow separation and reattachment processes are qualitatively congruent with experimental observation. Ou and Jameson [9] simulated a low Reynolds flow around plunging and pitching airfoils with deformation, separately and simultaneously. For this purpose, a high order Navier-Stokes solver, based on the spectral difference method, was used. They changed two parameters: the amount and location of maximum curvature, to deform the shape of the section. Then, the conditions of maximum thrust generation were obtained.

Since shear layers and, also, the vortices around the body surfaces become more important in the flow around the airfoil undergoing pitching motion, boundary layer growth and flow separation must be estimated properly. One way to prevent artificial boundary layer growth due to artificial viscosity is to apply the compressible surface vorticity confinement technique. In this method, a body force and the work done by this force are added as a source term to the momentum and conservation energy equations, respectively. A non-diffusive solution of the Euler equations with a non-slip boundary condition and coarse grid could be obtained. This technique reduces artificial viscosity, cancels vortex distribution and prevents the unrealistic growth of the boundary layer and separation region in coarse grids. The vorticity confinement theory was first introduced by Steinhoff [10] and Hu [11]. Further, Steinhoff used this method as a LES turbulent model [12]. It was improved and employed for different applications by Moulton and Steinhoff [13], Wenren et al. [14] and Dietz [15]. They indicated that by using this method, the vortex does not spread out over large distances and keeps its power. Also, the accuracy of the obtained results is close to RANS computations with less required computational time. Butsuntorn and Jameson [16] used this model for the flow around the propellers and wings of the helicopter and showed that this method is very effective in improving results. Initial works are finally completed with an arbitrary factor, called a confinement parameter, which must be determined by the user. This factor could be found, according to experimental results. Bagheri-Esfeh and Malek-Jafarian [17] implemented this method for different numerical dissipation schemes. They found that for each scheme, the confinement parameter could be estimated systematically instead of by trial and error. The vorticity confinement method was initially and extensively used to preserve vortex convection for long distances. But, fewer investigations were done in the field of preventing boundary layer growth and artificial boundary layer simulations. Therefore, using the vorticity confinement method to thoroughly investigate turbulent flows around pitching airfoils is one of the main specifications of the present paper.

Further, a particular adaptive grid method is required to simulate the motion. In the present work, a spring network analogy is employed with some refinements. The origin of this method is presented by Nakahashi and Deiwert [18] and Murayama et al. [19]. In this method, each mesh edge is replaced by a tensional spring, whose stiffness is inversely proportional to the edge length. To avoid possible collapse, they utilized torsional springs for each node. In the present work, secondary linear springs have been applied instead of torsional springs to prevent network collapse; a multi zone adaptive grid is also presented. This technique leads to a considerable reduction in computational time and has the ability to take large steps forward.

Therefore, in the present work, firstly, the unsteady two dimensional compressible flow around a pitching airfoil at a high Reynolds number is conducted in which oscillation amplitude is varied in the range of 1° to 11°, and the reduced frequency is changed between 0.133 and 1. Some of these unsteady parameters were investigated by other researchers, but the described method has the ability to calculate the same results for these parameters in extremely low computational time. Also, the effect of pitching axis position out of the airfoil section, which has been considered in this paper, has not yet been investigated by others. Secondly, Coarse Grid CFD (CGCFD) is applied to greatly reduce the computational time for pitching airfoils analysis. In this method, Euler equations are solved with a coarse grid and no slip boundary conditions with compressible surface vorticity confinement. It is well known that the time step and also the moving step of unsteady moving airfoils depend directly on the minimum mesh size in a computational domain. Therefore, to estimate real unsteady vortex patterns around the airfoils, it takes much time and cost, due to very fine grids adjacent to the airfoil wall required for viscous flow. Therefore, this numerical setup has the ability to achieve widespread results for unsteady cases in just one week, while the RANS computations need at least several months.

2. Numerical method

For the initial analysis, the general form of governing equations for 2-D compressible Navier-Stokes equations with a vorticity confinement source term is as follows:

$$\frac{\partial W}{\partial t}+\frac{\partial E_i}{\partial x}+\frac{\partial F_i}{\partial y}=\frac{\partial E_v}{\partial x}+\frac{\partial F_v}{\partial y}+S, \tag{1}$$

where W is the flow components, and F_i, E_i, F_v and E_v are inviscid and viscous flux vectors, respectively. Viscous flux vectors are eliminated for Euler equation solutions. S is also the vorticity confinement source term that will be defined later. Flow components and inviscid flux vectors are defined as follows:

$$W=\begin{bmatrix}\rho\\ \rho u\\ \rho v\\ \rho e\end{bmatrix}\qquad F_i=\begin{bmatrix}\rho(v-v_m)\\ \rho u(v-v_m)\\ \rho v(v-v_m)+P\\ \rho e(v-v_m)+Pv\end{bmatrix}$$

$$E_i=\begin{bmatrix}\rho(u-u_m)\\ \rho u(u-u_m)+P\\ \rho v(u-u_m)\\ \rho e(u-u_m)+Pu\end{bmatrix} \tag{2}$$

in which, ρ, E and P are the density, total energy and pressure, respectively, u and v are the velocity components in x and y directions, and u_m and v_m are also mesh velocities. By adding the velocity of the elements to the governing equations, according to Eq. (2), the condition of mass conservation will be satisfied [20].

In the following equations, H and P are obtained, in which H is the stagnation enthalpy, c is the sound velocity and γ is the specific heat ratio:

$$H=E+\frac{p}{\rho}=\frac{c^2}{\gamma-1}+\frac{u^2}{2},\qquad c^2=\frac{\gamma P}{\rho},$$

$$P=(\gamma-1)\rho(E-\frac{u^2}{2}). \tag{3}$$

Eq. (1) can be expanded in one-dimensional form as follows:

$$\Delta x\frac{dW_i}{dt}+F_{i+1/2}-F_{i-1/2}=0, \tag{4}$$

$$F_{i+1/2}=\frac{1}{2}(F_{i+1}+F_i)-d_{i+1/2}, \tag{5}$$

where $d_{i+1/2}$ is the dissipation term added to the governing equation to prevent oscillations and instabilities. This is the main reason for artificial boundary layer growth. Some schemes have calculated this term as a function of flow gradients and conditions. In this work, the SCalar Dissipation Scheme (SCDS) is applied to estimate this term. (For more information, see [21].)

The fourth order Runge-Kutta method is used for time stepping, in order to reach higher accuracy. Also, the Spalar-Allmaras turbulence model [22] is applied to the original code for the viscous solution.

2.1. Vorticity confinement

Compressible Vorticity Confinement (CVC) will be defined by adding a body force to the momentum equations, and its correlated work to the energy equation, in regions with high velocity gradient, like vortical zones or surface boundary layers. It results in reduction or omission of inherent dissipation related to the governing equations. The source term, S, is added to the Euler equations as a CVC function (Eq. (1)), whose components are defined as follows [14]:

$$\vec{S} = (0 \quad \rho\vec{f_b}.\hat{i} \quad \rho\vec{f_b}.\hat{j} \quad \rho\vec{f_b}.\vec{V}), \tag{6}$$

in which $\vec{f_b}$ is the body force per unit mass, which balances the diffusion of the numerical errors and the conservation of momentum in the high velocity gradient regions. This force produces a velocity vector toward the center of the vortex in fully separated regions or toward the solid walls in regions near body surfaces.

$$\vec{f_b} = -D_c\hat{n}_c \times \vec{\omega}. \tag{7}$$

E_c is the VC parameter that controls the power of confinement. VC can be applied in two distinct ways: field and surface confinements, which depend on the definition of the unit vector, n_c. The field confinement acts upon freely convecting vortical structures. n_c is defined as the normalized gradient of the vorticity vector magnitude. With surface confinement, n_c is the unit vector normal to the solid surfaces of the configuration. In this case, by adjustment of the confinement parameter, flow near a body surface remains attached against an adverse pressure gradient. As a result, surface confinement can be considered a simple implicit model for a turbulent boundary layer. The original form of VC in compressible flow solvers can be found in [10,15].

When numerical dissipation and VC are applied simultaneously, the right hand side of the Euler equations will be concluded as Eq. (9):

$$RHS = d_{i+1/2} + \rho E_c \omega_z \times \underbrace{\frac{\frac{\partial}{\partial x}|\omega_z|}{|\nabla|\omega_z||}}_{cons\tan t},$$

$$\omega_z = \frac{\partial v}{\partial x} - \frac{\partial u}{\partial y}. \tag{8}$$

The first term of this equation refers to numerical dissipation, and the second one is due to VC. Since, within the boundary layer, we have: $\frac{\partial v}{\partial x} \langle\langle \frac{\partial u}{\partial y}$, the VC term is negative, which leads to a reduction in numerical dissipation and artificial viscosity, thus preventing artificial boundary layer growth. In the boundary layer, VC becomes more important, because $\frac{\partial u}{\partial y}$ is large.

3. Multi zone adaptive grid

In this paper, when the airfoil boundary moves or rotates, the computational flow field meshes are refined by using a spring network analogy [18]. An advantage of using this technique is that the computer time required for running is reduced significantly. In this paper, the structured grid edges are replaced with linear springs, which are balanced in several iterates. A logical definition is assumed for linear spring coefficients and displacement of nodes.

For the first step of this analogy, each mesh edge is replaced by a spring, whose stiffness is inversely proportional to the edge length. In this way, longer edges will be softer, while shorter ones will be stiffer; this assumption somewhat prevents the collision of neighboring vertices. If the displacements are large, the edge spring method cannot prevent the creation of nearly flat elements, and will lead to the collapse of mesh networks. In order to avoid the possible collapse of grid networks, secondary linear springs have been also applied.

However, the fine grids suitable for the boundary layer will, most probably, collapse, specifically for meshes adjacent to walls. To avoid this problem, a multi zone adaptive grid is designed for the computational domain which is divided into three zones. The first zone, which is adjacent to the body, is rotating with the boundary and is regenerated in each time step. The second one includes an adaptive zone in which the mesh points are adapted for each time step. Finally, the third zone (outer region) is fixed and does not vary with time. It causes the grids in the adaptive zone to become coarser than those near solid walls and prevent the meshes from collapsing during the motion. These zones are shown in Figure 1.

4. Dynamic case study

The pitching airfoil is a NACA0015 airfoil with a flow field, with 0.3 Mach number and a Reynolds number equal to 2e6. Eq. (10) shows the sinusoidal variation of the passing and effective angle of attack as:

$$\alpha(t) = \alpha_m + \alpha_0 \sin(kt), \tag{9}$$

$$\alpha_{\text{eff}}(t) = \alpha(t) + \frac{c\dot{\alpha}}{}2U_\infty, \tag{10}$$

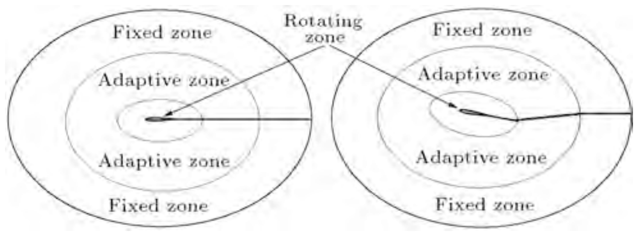

Figure 1. Multi zone adaptive grids.

Table 1. Mean angle of attack, the oscillation amplitude and the reduced frequency for validation cases.

Case	α_m	α_0	K	X_{cp}
Pitch 1	0.88	4.33	0.133	0.25
Pitch 2	4.02	4.33	0.133	0.25
Pitch 3	8.99	2.08	0.1	0.25

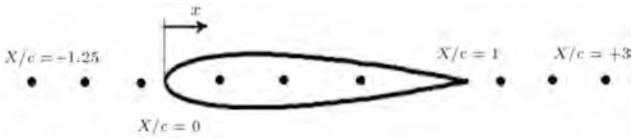

Figure 2. Schematic of the points for pitching axis position.

in which α_m, α_0 and $k = \omega c/U_\infty$ are the mean angle of attack, oscillation amplitude and reduced frequency, respectively, and also, $\alpha_{\text{eff}}(t)$ is the effective angle of attack [21]. The validation cases are shown in Table 1, and the computational results are compared to the experimental data in [2]. In each case, oscillation amplitude, reduced frequency and the position of pitching axis (X_{cp}) are changed and their effect on the aerodynamic coefficient is investigated.

Note that, to investigate the effect of the pitching axis position (X_{cp}), the positions are not limited to the points inside the airfoil. Some points are selected in front of the airfoil and some behind. The schematic of some points for the pitching axis position (X_{cp}) is shown in Figure 2. If the airfoil rotates around the outside points, there will be a specific combination of pitching and plunging motions simultaneously. It seems that this kind of motion has not been investigated by other researchers yet, whereas, having less computational time, it, will be considered deeply in this work.

It should be considered that flow around flapping airfoils can be simulated in two distinct ways: inlet flow oscillation with a fixed object or object movement (oscillation) in a constant flow. The object oscillation is employed because of high accuracy, low sensitivity, easy modeling and fast hysteresis curve convergence.

4.1. General algorithm

- Before flapping the airfoil, the solver allows the flow to become steady with the surface velocity and angle of attack at the middle of the oscillation ($t = 0$ in Eq. (12)). In this part of the solution, local time stepping is employed to speed up the initial steady solution. This technique leads to quick convergence of the unsteady aerodynamic coefficient loops.
- Then, the airfoil begins to pitch with a time accurate method, in which the time step is selected as the minimum calculated time step of the domain. In each step, using the lowest time step leads to complete data transfer in all elements. It must be mentioned that time step size can be obtained from the Courant number formulation. The motion step size then can be calculated by inserting the minimum time step of the whole domain in Eq. (10).
- After each time and motion step, the airfoil and its adjacent grids (rotating zone, Figure 1) are rotated. Therefore, grids on the intersection of rotating and adaptive zones will rotate. This results in disturbing the springs' equilibrium in the adaptive zone. Then, the grids in the adaptive region will be adapted with the motion.
- After adaption, data in all grids will be updated. Since the location of each grid point is changed in each step, the velocity of the mesh should be considered. To do this, the mesh velocities are applied to the governing equations (u_m and v_m in Eq. (2)). This is required to satisfy the mass conservation condition.

5. Results and discussion

5.1. Boundary condition

Inlet u and v components of velocity are equal to free stream velocity, while inlet pressure p and density ρ are computed from energy and state equations. Outlet velocities and density are extrapolated from the flow, and outlet pressure is assumed equal to free stream pressure. A no-slip boundary condition is also selected for the solid wall condition. Therefore, the velocity on the solid surface is equal to the airfoil velocity and can be computed from Eq. (11):

$$u\Big|_{y=y_s} = r\sin\theta\frac{d\alpha}{dt} = rK\alpha_0 Cos(Kt)\sin(\theta-\alpha(t))$$

$$v\Big|_{y=y_s} = -r\cos\theta\frac{d\alpha}{dt} = -rK\alpha_0\cos(Kt)\cos(\theta-\alpha(t)), \tag{11}$$

in which y_s is related to the points adjacent to the wall. r and θ are distance and angle of the points on the solid surface to the center of pitching, and $\alpha(t)$ can be obtained from Eq. (10). The pressure and density on the solid wall are extrapolated from the inside of the flow.

5.2. Grid selection

For the investigation of mesh independency and selecting grid size, flow around a fixed airfoil at zero angle of incidence is simulated, and the computed lift coefficient is summarized in Table 2.

The grid size is selected 160×90, because finer grids do not result in considerable variations in lift coefficient, but require much higher computational cost. The selected mesh is indicated in Figure 3.

Table 2. Mesh independency in tangential (i) and normal (j) direction.

Variation of grid size in j direction	Cl	Variation of grid size in i direction	Cl
100 × 70	0.0336	140 × 90	0.00732
100 × 80	0.0207	**160 × 90**	**0.00602**
100 × **90**	**0.00951**	180 × 90	0.00588
100 × 100	0.00896	200 × 90	0.00555

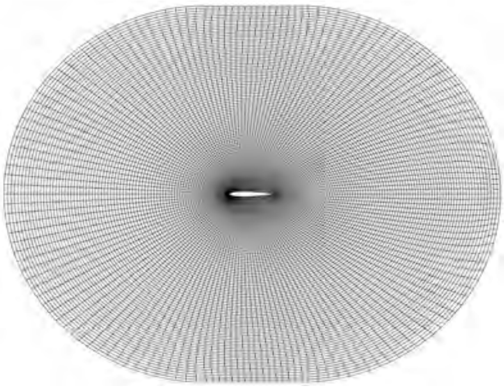

Figure 3. Computational grid network.

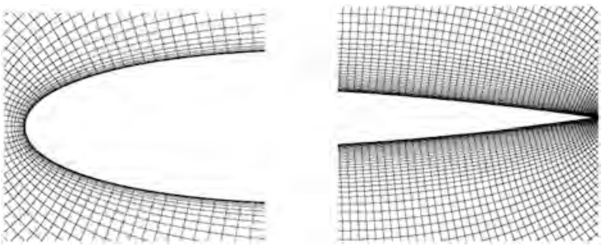

Figure 4. Mesh elements near solid wall for RANS simulation.

The appropriate grid for viscous simulations is generated with respect to the following points: Firstly, the computational grid is produced by solving a two dimensional Poissan equation. Thus, an approximately orthogonal grid network is generated for the region adjacent to the airfoil body surface. The grid mesh can be observed from Figure 4. Secondly, 20 elements are added to the selected inviscid grids across the boundary layer. Thirdly, $Y+$ keeps less than 5 in RANS simulation. Therefore, the mesh number along the surface is the same as the inviscid one (160 grids). But, the mesh number is equal to 110 elements instead of 90 in the normal direction.

5.3. Validation

First, the accuracy of the described method (Coarse Grid CFD) is examined in comparison with the results of RANS, with a fine grid, a one-equation Spalart-Allmaras turbulence model, and also, the experimental data in [2]. To perform this, the conditions,

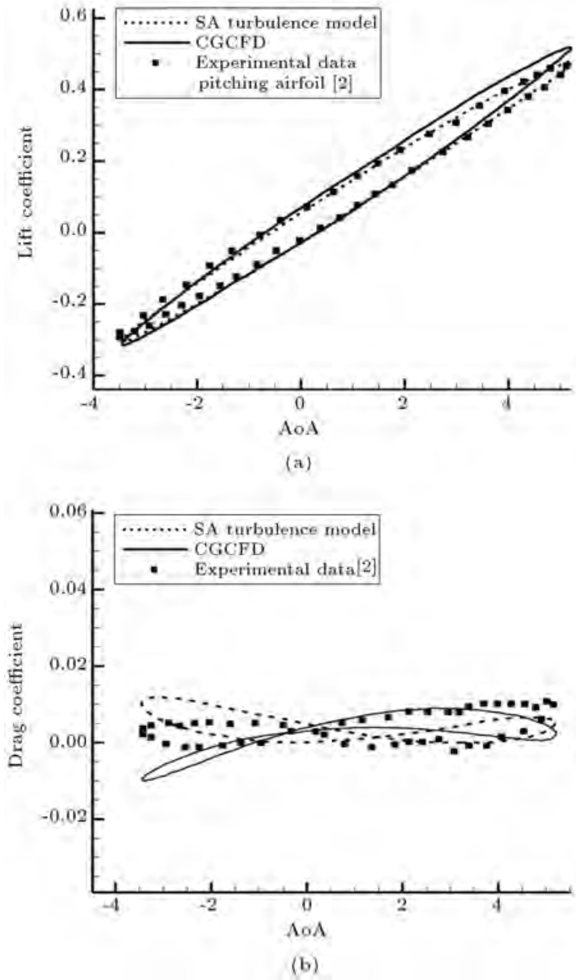

Figure 5. Comparing the results of aerodynamic coefficients versus Angle of Attack (AoA): (a) Lift coefficient; and (b) drag coefficient ($k = 0.133$,, $\alpha_0 = 4.33$ and $\alpha_m = 0.88$).

which have been demonstrated in Table 1, are added to the code, and the results are evaluated as follows.

As can be seen in Figure 5(a) $k = 0.133$, $\alpha_0 = 4.33$ and $\alpha_m = 0.88$, the lift coefficient, obtained using the CGCFD method, matches well with experiments, but, a slight deviation at the top and bottom of the oscillation is perceived. In Figure 5(b), when the flow encounters the lower surface of the airfoil, the drag coefficient is estimated close to the experiments. By changing the flow incidence direction from the lower to the upper surface, the results deviate from experimental data. The changing point of the flow incidence direction is calculated correctly. The summary of calculated average lift and drag coefficients is illustrated in Table 3.

Figure 6 indicates the results of lift and drag coefficients versus angle of attack in comparison with experiments for $k = 0.133$, $\alpha_0 = 4.33$ and $\alpha_m = 4.02$. Lift coefficients agree well with experiments, but drag

Table 3. Comparison of mean aerodynamic coefficients and errors ($k = 0.133$, $\alpha_0 = 4.33$ and $\alpha_m = 0.88$).

	Cl	**Error of Cl**	**Cd**	**Error of Cd**	**Time (hour)**
RANS	0.116	21.9%	0.00453	9.7%	168
CGCFD	0.0995	12.5%	0.00943		3
Experiments	0.0884		0.00497		

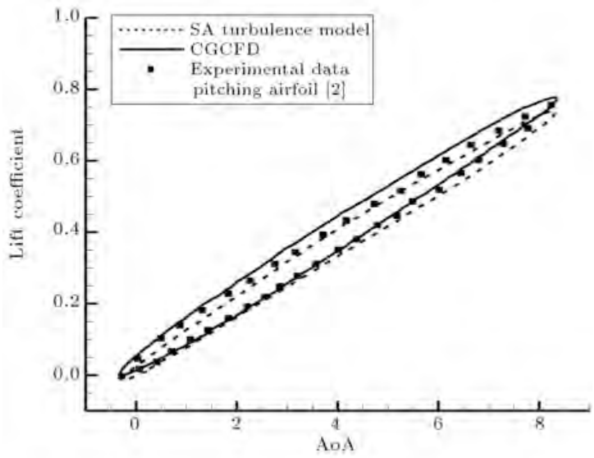

(a)

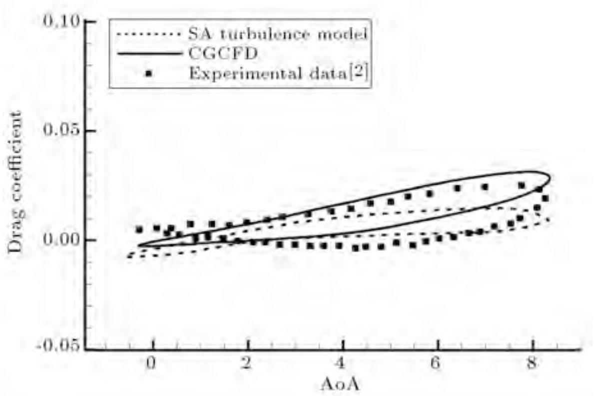

(b)

Figure 6. Comparing the results of aerodynamic coefficients versus Angle of Attack (AoA): (a) Lift coefficient; and (b) drag coefficient ($k = 0.133, \alpha_0 = 4.33$ and $\alpha_m = 4.02$).

Table 4. Comparison of mean aerodynamic coefficients ($k = 0.133$, $\alpha_0 = 4.33$ and $\alpha_m = 4.02$).

	Cl	**Error of Cl**	**Cd**	**Error of Cd**	**Time (hour)**
RANS	0.386	10.9%	0.00403	41.01%	168
CGCFD	0.385	10.6%	0.01018	49.7%	3
Experiments	0.348		0.00684		

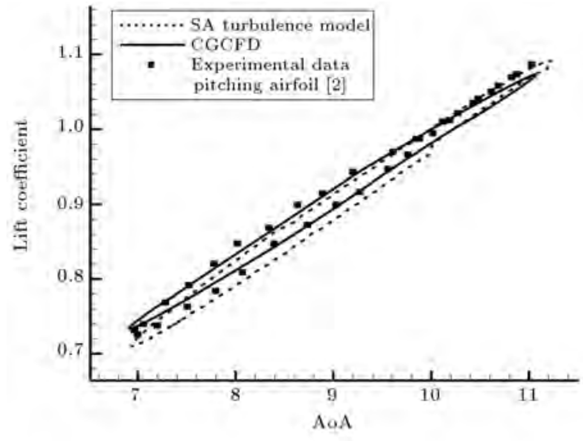

(a)

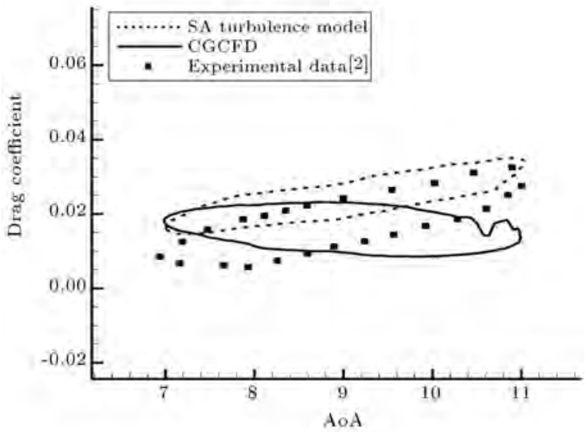

(b)

Figure 7. Comparing the results of aerodynamic coefficients versus Angle of Attack (AoA): (a) Lift coefficient; and (b) drag coefficient ($k = 0.1, \alpha_0 = 2.03$ and $\alpha_m = 8.99$).

coefficients deviate a little from experiments at the bottom of the oscillation. In Table 4, the results of average lift and drag coefficients are summarized.

In Figure 7, obtained lift and drag coefficients are compared with experiments for $k = 0.1$, $\alpha_0 = 2.03$ and $\alpha_m = 8.99$. Lift and drag coefficients are approximately close to the experiments, except at the top of the oscillation. The results of average lift and drag coefficients are compared in Table 5.

According to the preceding consequences, the RANS solution, with a fine grid and a one-equation Spalart-Allmaras turbulence model, computes the hysteresis loops and average coefficients accurately, but, high computational time is required. Results of the Coarse Grid CFD method are acceptable for lift and drag coefficients, particularly at low and moderate angles of attack. However, in passing low angles of attack, a little difference can be perceived in drag coefficient. As can be observed, although the CGCFD method calculates the mean drag coefficient inaccurately, especially for low mean angles, the trend of the obtained hysteresis loop is close to experiments.

Table 5. Comparison of mean aerodynamic coefficients ($k = 0.1$, $\alpha_0 = 2.03$ and $\alpha_m = 8.99$).

	Cl	Error of Cl	Cd	Error of Cd	Time (hour)
RANS	0.8993	3.7%	0.0271	53.78%	168
CGCFD	0.9192	1.6%	0.0278	62.5%	3
Experiments	0.9342		0.0171		

However, because of very low required computational time, the CGCFD method has a major advantage to be employed. To investigate the influence of unsteady parameters, this method assists in performing more runs in the lowest possible time. Since, it takes only three hours for one loop oscillation in each run, with a Corei5 Cpu and 4 Gigabite Ram computer system, three to four days are enough to do all the runs needed in this paper. While, if the RANS computation with a conventional fine grid is used with the same computer system, it will take about one week for one loop of oscillation in each run. Thus, to obtain these results, the computational time will take at least several months. Therefore, the Coarse Grid CFD method can be applied as a quick and acceptable technique to estimate the approximate aerodynamic behavior of unsteady flapping airfoils under greatly varying conditions.

Although the results of lift and flow patterns are estimated well with this method, considerable deviations from experiments are observed for drag and boundary layer calculations. Therefore, the results show that using CGCFD to find lift coefficient is more reasonable, while it is not appropriate for accurately calculating drag forces. The main reason is related to predicting the pressure distribution well with the CGCFD method, which can be observed from Figure 8. However, it is possible to reliably predict the trend and variation of drag forces by applying the CGCFD method.

The pressure coefficient of a fixed airfoil at a 6° angle of attack and pitching airfoil passing this angle in a downward and upward motion is shown in Figure 8. This figure shows that the pressure distribution along the airfoil is estimated well.

5.4. *Effects of unsteady parameters for $\alpha_m = 0.88°$*

In the first case, for the mean angle of attack equal to 0.88°, oscillation amplitude is set at 4° to 11°. Reduced frequency is varied between 0.133 and 1, and the position of the pitching axis is varied between -1.25 to +3.

5.4.1. Variation of oscillation amplitude (α_0)

Figure 9(a) points out that the hysteresis loop of lift coefficient versus angle of attack becomes slightly

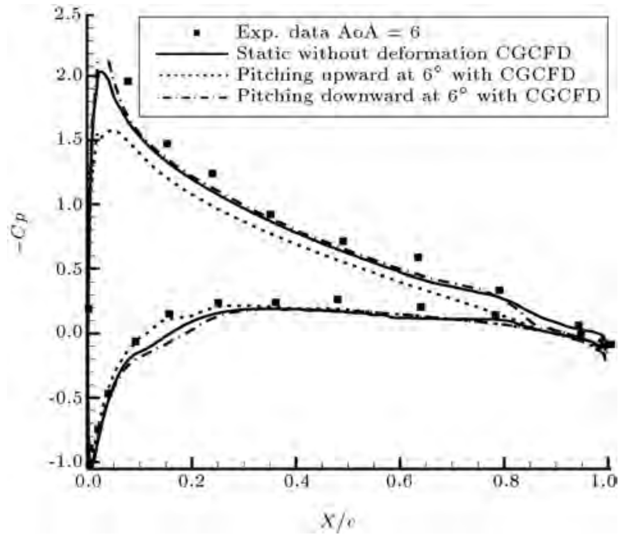

Figure 8. Comparison of pressure coefficient on fixed and pitching airfoil at 6° angle of attack.

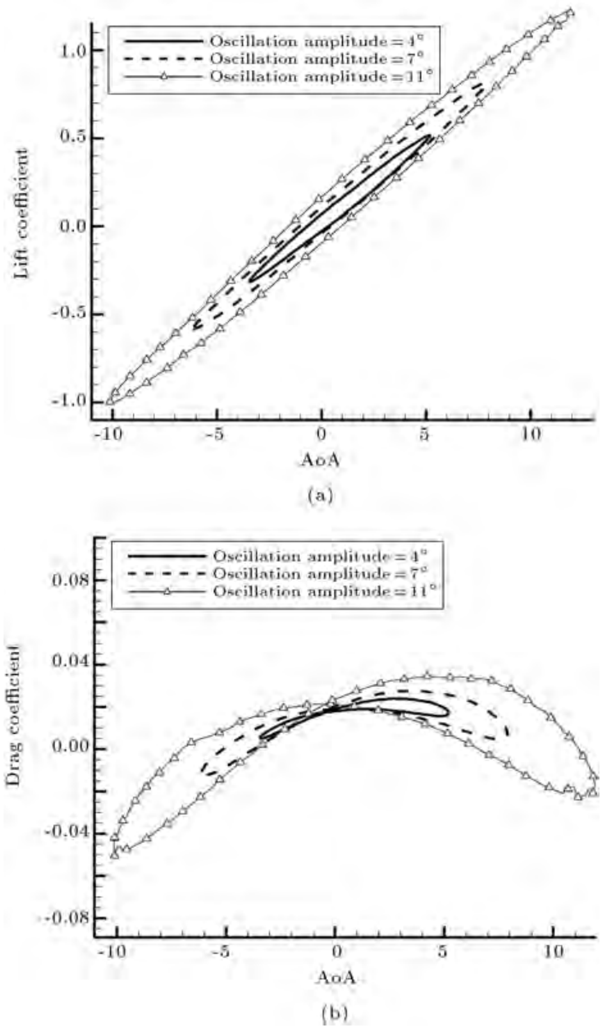

Figure 9. Effect of oscillation amplitude on aerodynamic coefficients versus angle of attack: (a) Lift coefficient; and (b) drag coefficient ($k = 0.133, X_{cp} = 0.25$ and $\alpha_m = 0.88°$).

broadened by increasing the oscillation amplitude. But, the slope of the loop does not change. The main reason for these behaviors is the coefficient α_0 in Eq. (12). It leads to increasing the wall velocity and effective angle of attack (α_{eff}), except at the top and bottom of the cycle. Since the upper line of the curve is related to the down-stroke and the lower line refers to the upward phase of motion, the variation of lift coefficient with oscillation amplitude at the down-stroke stage is more than at the up-stroke stage. From Figure 9(b), it can be seen that up and down-stroke curves intersect each other at a point that refers to the effective angle of attack, in which the flow incidence direction changes from the lower to the upper surface. It results in a bow tie shape for the hysteresis drag curve. Increasing the oscillation amplitude is ineffective on the position (angle) of the intersection point. In high oscillation amplitudes, for example, $\alpha_0 = 11°$, some fluctuations in drag coefficient can be detected at the top and bottom of the oscillation cycle. The reason is the interaction of the low pressure zones moving on the upper surface of the airfoil in the up-stroke stage and also of those zones existing on the lower surface in the downward motion.

It can be seen that by enhancing the oscillation amplitude, the maximum of the lift coefficient is increased and the minimum comes down. This figure indicates that variations in maximum drag coefficient are negligible in comparison with changes in, the lowest one. Increasing the oscillation amplitude leads to a reduction in minimum drag coefficient.

5.4.2. Variation of pitching axis position (X_{cp})

Figure 10 investigates the effect of pitching axis position on the lift and drag coefficient for $k = 0.133$, $\alpha_0 = 4.33°$ and $\alpha_m = 0.88$. As can be seen in Figure 10(a), by displacing the pitching center to the right hand side (positive positions) and distancing from the trailing edge (its schematic is illustrated in Figure 2), the counter clockwise hysteresis loop of lift coefficient versus angle of attack is considerably broadened. According to Eq. (12), by increasing the distance of the pitching axis position from the surface (increasing in r), the wall velocity is increased. Since the surface and incoming flow velocities relatively strengthen each other in a downward motion, the effective angle of attack and lift coefficient are increased. In the upward motion, they stepped down from each other and the effective angle of attack and lift coefficient are reduced. Thus, the loop is widened. The maximum lift coefficient is slightly increased and the minimum one is fixed. In Figure 10(a), by moving the pitching axis position to the left side (negative positions) and distancing from the leading edge, the inverse of the above observations is occurred. The effective angle of attack and lift

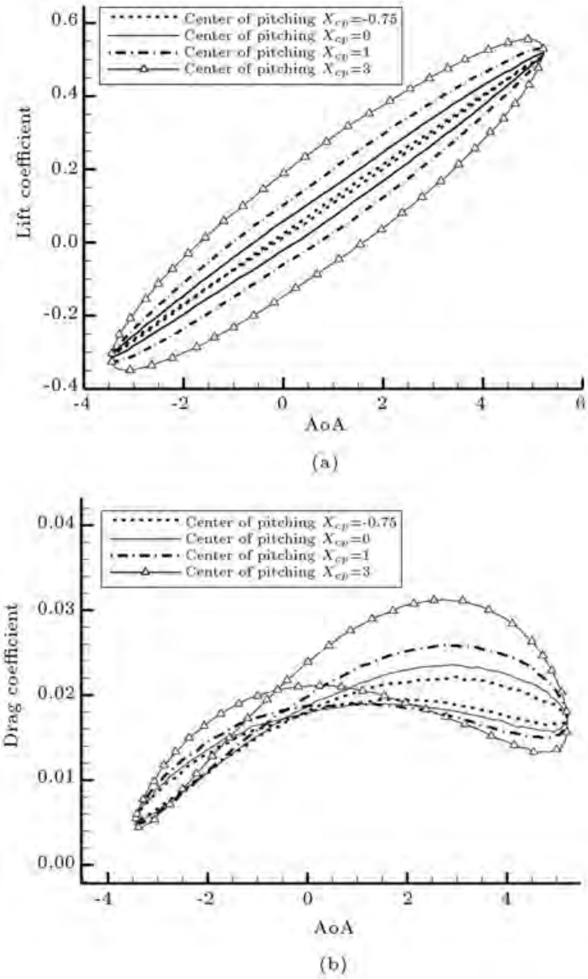

Figure 10. Effect of pitching axis position on aerodynamic coefficients: (a) Lift coefficient; and (b) drag Coefficient (($k = 0.133, \alpha_0 = 4.33°$ and $\alpha_m = 0.88°$).

coefficient are decreased in the downward motion, but enhanced in the upstroke, leading to a narrower loop. In $X_{cp} = -0.75$, up-stroke and down-stroke curves coincide by further increasing the distance from the leading edge. Then, in $X_{cp} = -1.25$, the up-stroke curve, which was further down, ascends to the top of the down-stroke curve and the hysteresis loop direction changes to clockwise.

In Figure 10(b), the effect of pitching axis position on drag coefficient for $k = 0.133$, $\alpha_0 = 4.33°$ and $\alpha_m = 0.88$ is investigated. Figure 10(b) shows that by changing the position of the pitching center to the right hand side (positive positions), and displacing from the trailing edge, the hysteresis loop of drag coefficient moves up and the intersect point inclines to lower angles of attack. In this case, the maximum drag coefficient is increased, whereas the minimum one is fixed. In Figure 10(b), by moving the pitching axis position to the left hand side (negative positions) and going far from the leading edge, the maximum drag coefficient is reduced, while the minimum one is still fixed. In positive positions, both parts of the curve related to the flow incidence to lower and upper surfaces are influenced. But, in negative places, just the curve part related to the flow incidence to the lower surface is affected. Changing the drag hysteresis loop direction can be observed at position $X_{cp} = -0.75$. From Figure 10, the lift and drag coefficients related to the top and bottom of the cycle are not affected by moving the pitching axis position. Because, in these points, $\cos(Kt)$ is equal to zero (Eq. (12)), the surface velocities vanish.

5.4.3. Variation of reduced frequency (k)

Figure 11 shows the effect of reduced frequency (k) on mean aerodynamic coefficients for $X_{cp} = 0.25$, $\alpha_0 = 4.33°$ and $\alpha_m = 0.88$. Variation of k to less than 0.2, approximately, does not affect the aerodynamic coefficients. In Figure 11(a), increasing oscillation frequency causes a reduction in the slope of the lift coefficient hysteresis curve. At first, this curve is broadened, and then become narrow. This behavior is the consequence of the term $k \times Cos(kt)$ in Eq. (12). Figure 11(b) shows that large reduced frequencies lead to moving up and expansion of the drag bow tie shape. The intersection point of curves inclines to lower angles at low frequencies.

Note that, further increasing the reduced frequency from $k = 1$ ensures that the hysteresis loops of oscillations do not coincide with each other. The reason is the influence of the last previous period of oscillation loop on the present one at high frequencies.

From Figure 11, it can be also realized that increasing the reduced frequency results in decreasing the maximum and enhancing the minimum lift coefficient. Therefore, the difference between highest and lowest lift coefficients is decreased. Also, it eliminates minus lift coefficients and produces positive ones. This figure shows that enlarging the reduced frequency leads to increasing the maximum and minimum drag coefficients.

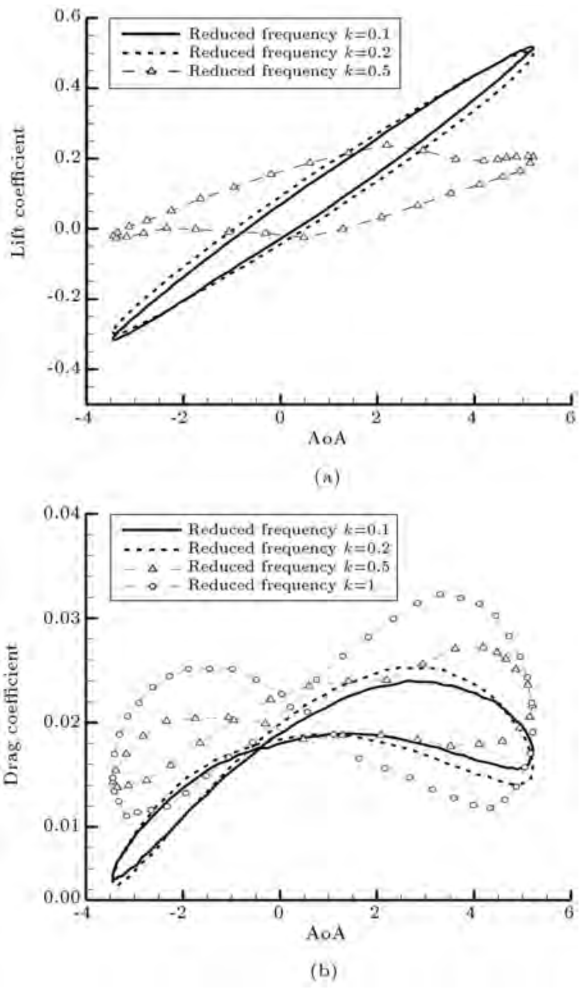

Figure 11. Effect of reduced frequency on aerodynamic coefficients: (a) Lift coefficient; and (b) drag coefficient ($X_{cp} = 0.25$, $\alpha_0 = 4.33°$ and $\alpha_m = 0.88°$).

5.5. *Effects of unsteady parameters for $\alpha_m = 4.02°$*

In the second case, for mean angle of attack equal to 4.02°, oscillation amplitude is set at 1° to 11°. Then, in the condition of flow attachment to the surface at $\alpha_0 = 4°$, reduced frequency is varied between 0.133 and 1, and the position of the pitching axis is changed from -1.25 to +3.

5.5.1. Variation of oscillation amplitude (α_0)

According to Figure 12, by increasing the amplitude of oscillation, the same results as $\alpha_m = 0.88°$ are obtained, until $\alpha_0 = 11°$, where a deep reduction in lift and an increase in drag coefficient are observed. This intense variation is caused by the large flow separation and vortex shedding from the backside of the airfoil at the top of the cycle (Figure 13). From Figure 12(b), it can be seen that the bow tie shape of the drag hysteresis loop is wiped out, and no intersection point occurs in low and moderate oscillation amplitudes. A poor intersection point can be observed in an angle near the bottom of the cycle by increasing the oscillation amplitude.

Figure 12 also indicates that the maximum of lift and drag coefficients are increased while the minimum ones are reduced by enhancing the oscillation amplitude. For $\alpha_0 = 11°$, intense reduction in lift and an increase in drag coefficients are observed at the top of the cycle.

In Figure 13, vorticity contours (a) and velocity contours (b) near the surface are shown at the top of the cycle for oscillation amplitude equal to 11°. As can be observed, the main reason for the intense reduction in lift and increase in drag coefficient is the vorticity production and the separation zone near the solid wall. The vortices are produced and detached because of the high effective angle of attack (α_{eff}) when the airfoil reaches the top of the cycle and begins to move downward. After flow reattachment to the airfoil surface, drag and lift coefficients are increased and returned to the hysteresis loop path.

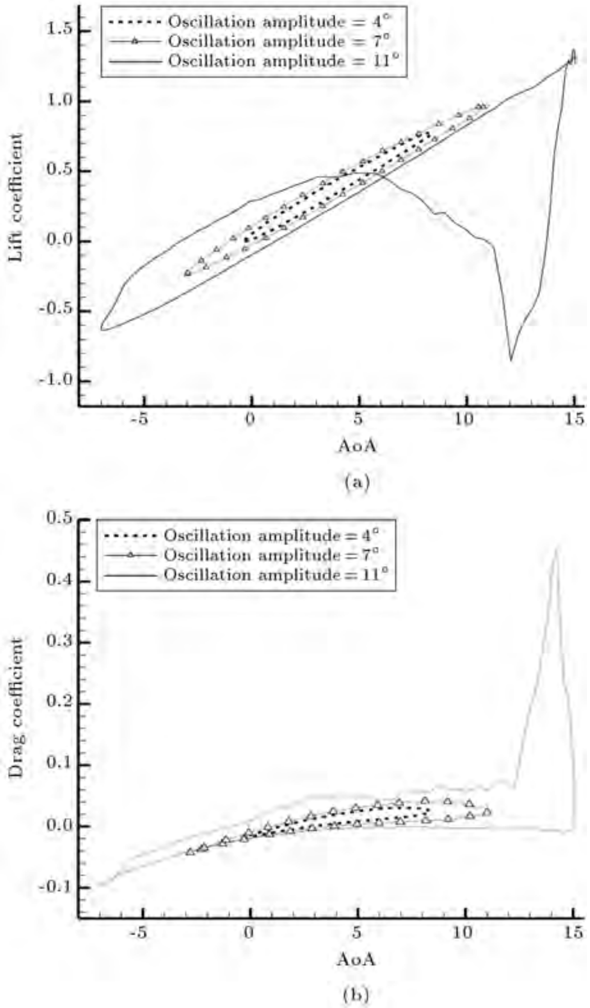

Figure 12. Effect of oscillation amplitude on aerodynamic coefficients versus angle of attack: (a) Lift coefficient; and (b) drag coefficient ($k = 0.133$, $X_{cp} = 0.25$ and $\alpha_m = 4.02°$).

5.5.2. Variation of pitching axis position (X_{cp})

Figure 14(a) shows that, by comparing the results of $\alpha_m = 4.02°$ and $\alpha_m = 0.88°$, the same consequences are obtained for lift coefficient. Positive positions and distancing from the trailing edge leads to broadening the lift hysteresis loop. But, negative positions and displacing from the leading edge results in a contraction of the lift hysteresis curve, inasmuch as the loop direction changes to clockwise.

In Figure 14(b), it can be observed that the consequences are the same as observations for $\alpha_m = 0.88°$ for drag coefficient. A little difference in the shape of the hysteresis loop and the intersection point can be seen. Positive places and distancing from the trailing edge leads to increasing maximum drag coefficient with no variation in minimum drag. Negative locations and going far from the leading edge result in decreasing the highest drag coefficient with no change in the lowest drag.

5.5.3. Variation of reduced frequency (k)

The effect of reduced frequency on aerodynamic coefficients for $X_{cp} = 0.25$, $\alpha_0 = 4.33°$ and $\alpha_m = 4.02°$ is indicated in Figure 15. Because of the increase in reduced frequency, the slope of the lift coefficient hysteresis curve is reduced, and the loop is broadened. The reason for this behavior is $k \times Cos(kt)$ in Eq. (12). Changing the values of k to less than 0.2, approximately, does not affect the aerodynamic coefficients. For higher values than 0.2, increasing the reduced frequency leads to decreasing the maximum and enhancing the minimum lift coefficient. It also increases the highest and lowest drag coefficient. In Figure 15(b), for $k = 1$, the maximum drag coefficient is reduced, and an intersection point is formed near α =1.5° (bow tie shape). At high frequencies, the highest and lowest lift coefficients do not occur at the top and bottom of the oscillation, respectively. The main reason is the influence of the flow field

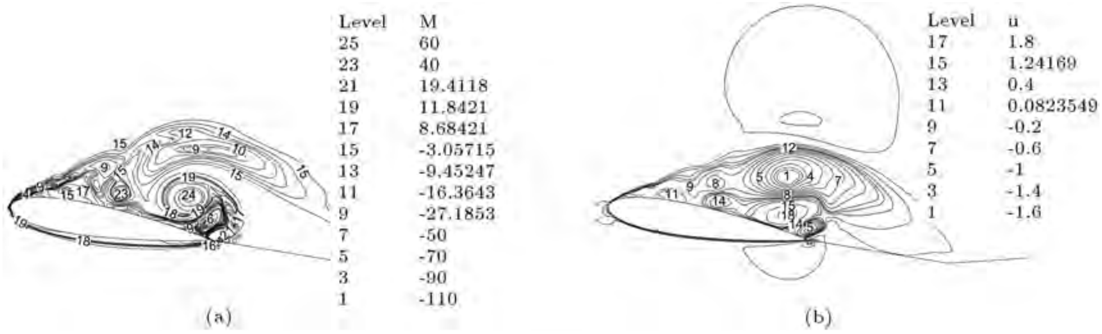

Figure 13. (a) Vorticity and (b) velocity contours near the surface in the top of the oscillation ($k = 0.133$, $X_{cp} = 0.25$, $\alpha_m = 4.02°$ and $\alpha_0 = 11°$).

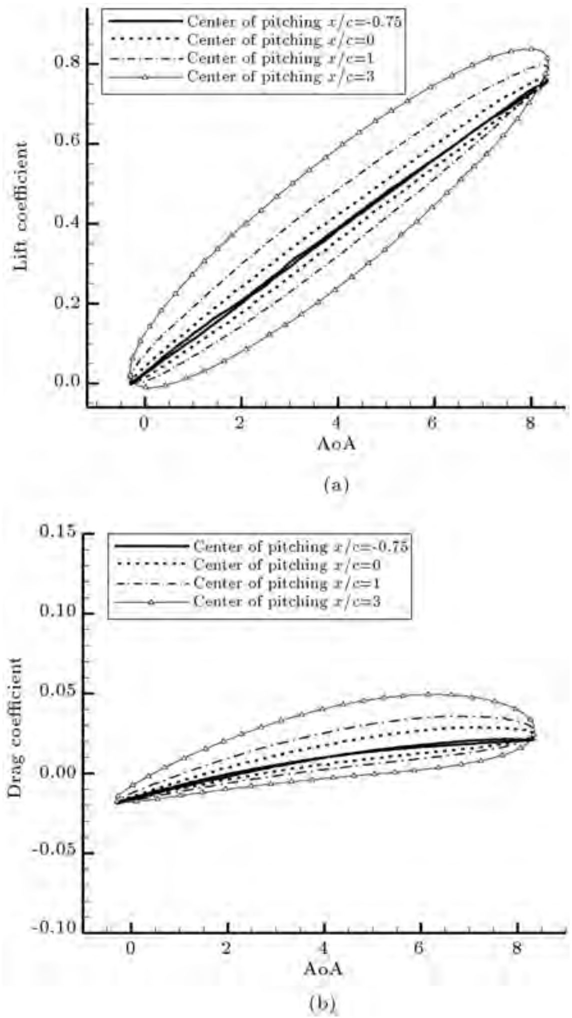

Figure 14. Effect of pitching axis position on aerodynamic coefficients versus angle of attack: (a) Lift coefficient; and (b) drag coefficient ($k = 0.133$, $\alpha_0 = 4.33°$ and $\alpha_m = 4.02°$).

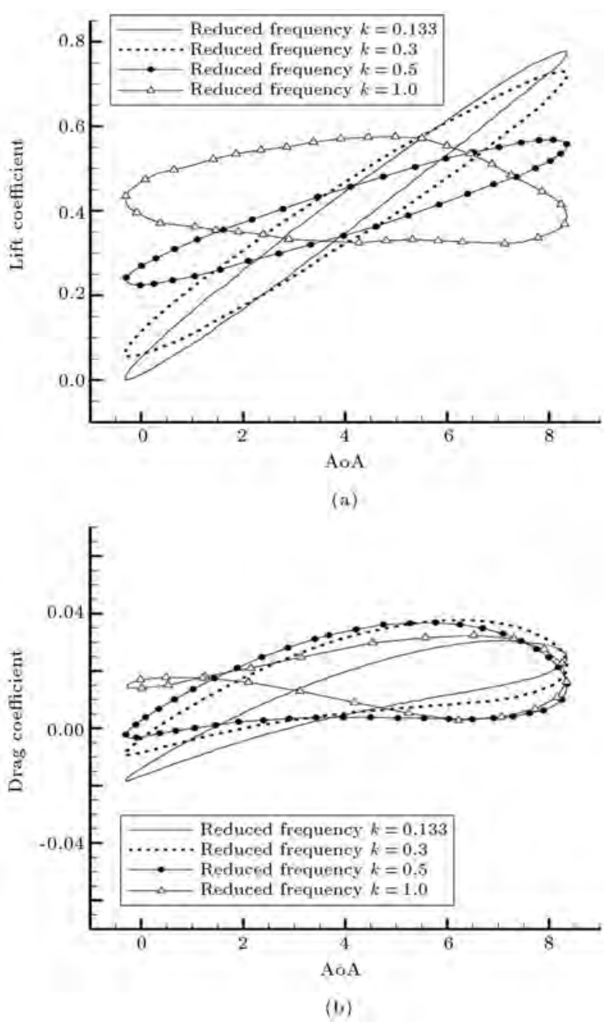

Figure 15. Effect of reduced frequency on aerodynamic coefficients versus angle of attack: (a) Lift coefficient; and (b) drag coefficient ($X_{cp} = 0.25$, $\alpha_0 = 4.33°$ and $\alpha_m = 4.02°$).

related to the last oscillation period on the present one.

5.6. Effect of unsteady parameters for $\alpha_m = 8.99°$

In this case, for mean angle of attack equal to 8.99°, oscillation amplitude is varied from 1° to 11°. Then, under the condition of flow attachment to the surface at $\alpha_0 = 4°$, reduced frequency is set between 0.133 and 1, and the position of the pitching axis is changed from -1.25 to +3.

5.6.1. Variation of oscillation amplitude (α_0)

In Figure 16, before $\alpha_0 = 6°$, the shape of lift and drag hysteresis loops are regular with no fluctuations. By increasing the amplitude of oscillation from 6° to 11°, and vortex shedding from the airfoil back side (Figure 17), some fluctuations and intense variations at the top of the stroke can be observed. When the oscillation amplitude is set at $\alpha_0 = 6°$, at the top of the motion (when $\sin(kt) = 1$ in Eq. (10)), when the angle of attack reaches 15°, the back side vortex detaches from the surface, and the low pressure region is replaced with a high pressure one. Then, a deep reduction in lift coefficient and an intense increase in drag coefficient occur. In low passing angles, when the flow reattaches to the surface, the curves approach the main hysteresis loops. This event takes place in the case of $\alpha_m = 4.02°$, with $\alpha_0 = 11°$ (Figure 12(a)), where the passing angle of attack at the top of the oscillation was equal to 15°, as well. Higher oscillation amplitudes lead to more powerful vortex shedding and more intense fluctuations in lift and drag coefficients at the top of the stroke.

Vorticity contours around the airfoil at the top of the stroke, while it passes the total angle of attack equal to 15°, is shown in Figure 17. As can be perceived, a strong vortex shedding occurs, which is the basis

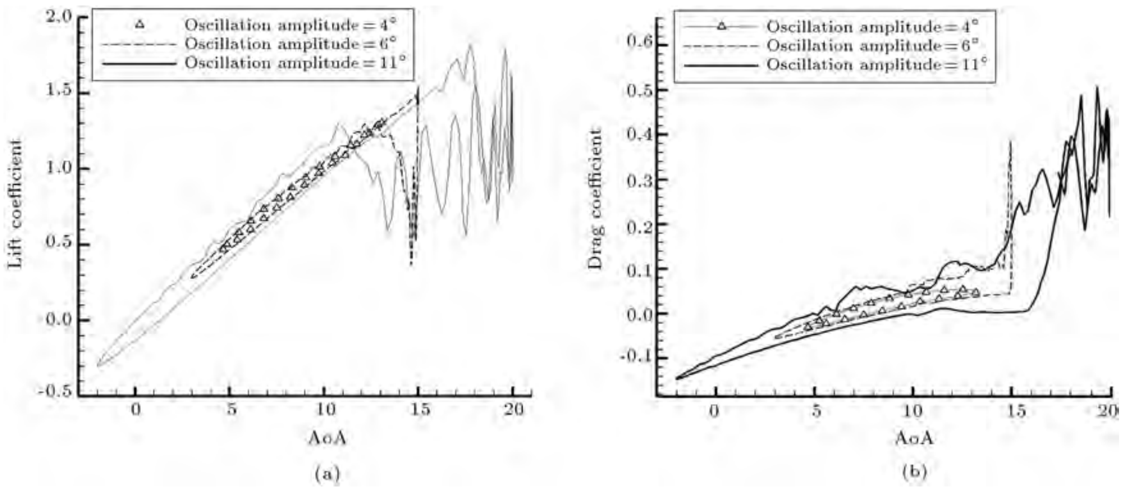

Figure 16. Effect of oscillation amplitude on aerodynamic coefficients versus angle of attack: (a) Lift coefficient; and (b) drag coefficient ($k = 0.133$, $X_{cp} = 0.25$ and $\alpha_m = 8.99°$).

Figure 17. Vorticity contours around the airfoil in the top of the oscillation ($k = 0.133$, $X_{cp} = 0.25$, $\alpha_m = 8.99°$ and $\alpha_0 = 11°$).

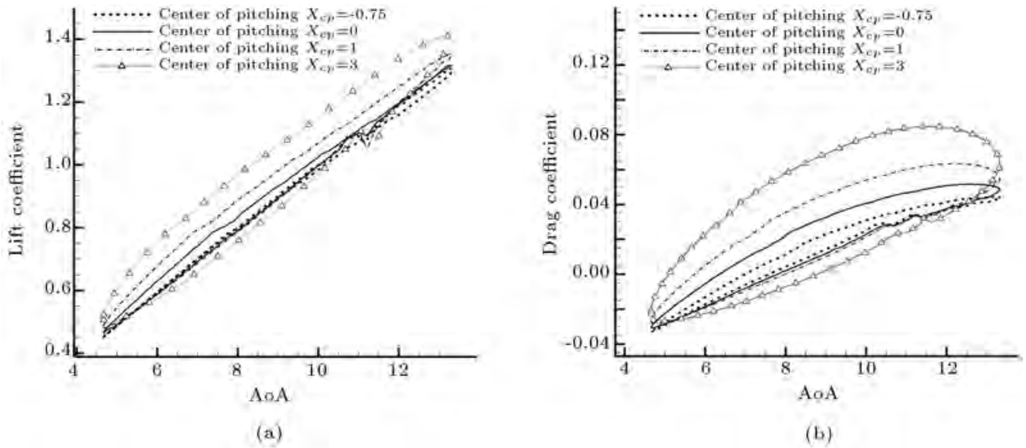

Figure 18. Effect of pitching axis position on aerodynamic coefficient versus angle of attack: (a) Lift coefficient; and (b) drag coefficient ($k = 0.133$, $\alpha_0 = 4°$ and $\alpha_m = 8.99°$).

of fluctuations and intense variations in aerodynamic coefficients at the top of the motion.

According to Figure 18(a), it can be observed that positive pitching axis positions lead to broadening the lift hysteresis loop, as before. It can be concluded that at high mean angles of attack (like $\alpha_m = 8.99°$), expansion of the hysteresis loop is only due to variations of lift coefficient in the down stroke. Changing lift coefficients in the upstroke is worthless in comparison with downward motion. Figure 18(a) also indicates that negative pitching axis positions result in a contraction of the lift hysteresis loop and a change in direction, as previous observations. The curve related to the upward movement does not change, due to displacement of the pitching center. But, the downstroke curve is moved from the upside of the loop

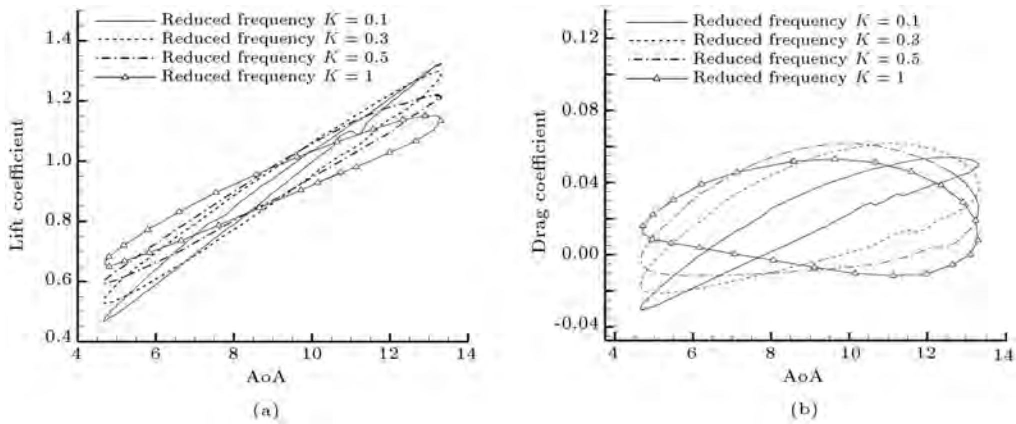

Figure 19. Effect of reduced frequency on aerodynamic coefficients versus angle of attack: (a) Lift coefficient; and (b) drag coefficient ($X_{cp} = 0.25$, $\alpha_0 = 4°$ and $\alpha_m = 8.99°$).

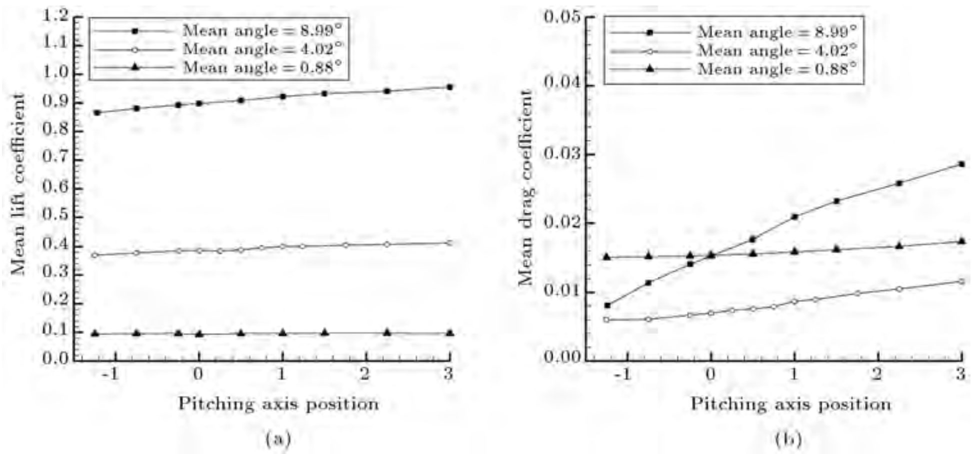

Figure 20. Effect of pitching axis position on mean aerodynamic coefficients: (a) Average lift coefficient; and (b) average drag coefficient ($k = 0.133$, $\alpha_0 = 4°$).

in $X_{cp} = 0$ to underneath in X_{cp} = -1.5. It leads to a change in the direction of the hysteresis loop to clockwise.

Figure 18(b) indicates that positive pitching axis positions result in increasing the maximum drag coefficient, while the lowest point is approximately fixed. Also, the highest drag points incline to the lower angles. For negative positions, also, the trend is the same, as when the axis point centers at points too far in front of the leading edge, the difference between up-stroke and down-stroke stages diminishes.

It can be perceived from Figure 19(a), by enlarging the reduced frequency, the hysteresis lift loop is widened, and the slope of the loop is decreased. Also, maximum lift is reduced and the minimum one is increased. Figure 19(b) illustrates that while the reduced frequency is enlarged, the highest drag is enhanced. Then, it is decreased in $k = 1$ and the lowest one is increased. Comparing this figure with Figure 15, it can be deduced that at lower mean angles, changing the reduced frequency affects the hysteresis loop of the aerodynamic coefficients considerably.

5.7. *Unsteady parameters effects on average aerodynamic coefficients*

According to Figure 20, using positive position centers and distancing from the trailing edge into the back of the airfoil, average drag coefficient can be increased slightly. However, it will be reduced, due to negative places and displacing from the leading edge in front of the airfoil. Also, the same results can be observed for average lift coefficient at $\alpha_m = 8.99°$. Variations of pitching axis position do not affect the average lift coefficient in lower mean angles ($\alpha_m = 0.88°$ and $\alpha_m = 4.02°$). It is interesting that for low mean angles of amplitude, the mean drag coefficient is nearly constant and is not a function of pitching axis position.

From Figure 21(a), it can be observed that variation of reduced frequency has a slight effect on average lift coefficient. Figure 21(b) shows that the minimum average drag coefficient can be achieved in low reduced frequencies (less than $k = 0.2$). Reduced frequencies above $k = 0.4$ lead to too high mean drag coefficients and are not recommended.

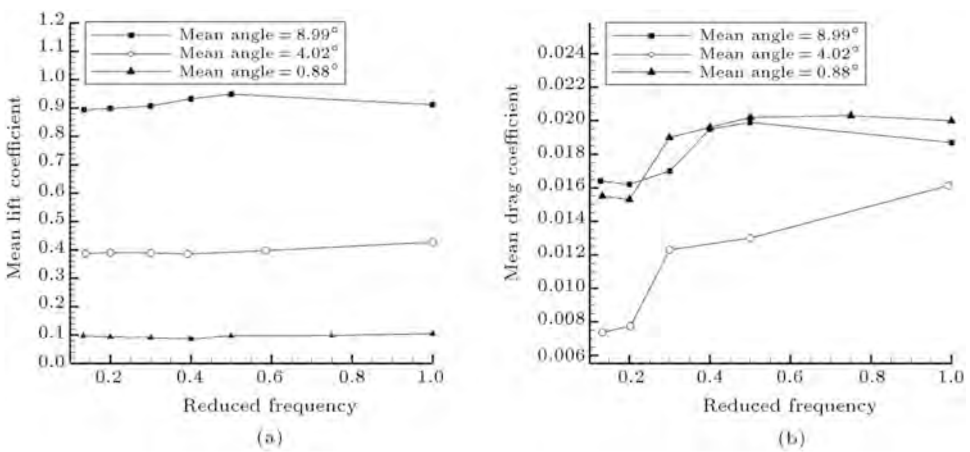

Figure 21. Effect of reduced frequency on mean aerodynamic coefficients: (a) Average lift coefficient; and (b) average drag coefficient ($X_{cp} = 0.25$, $\alpha_0 = 4°$).

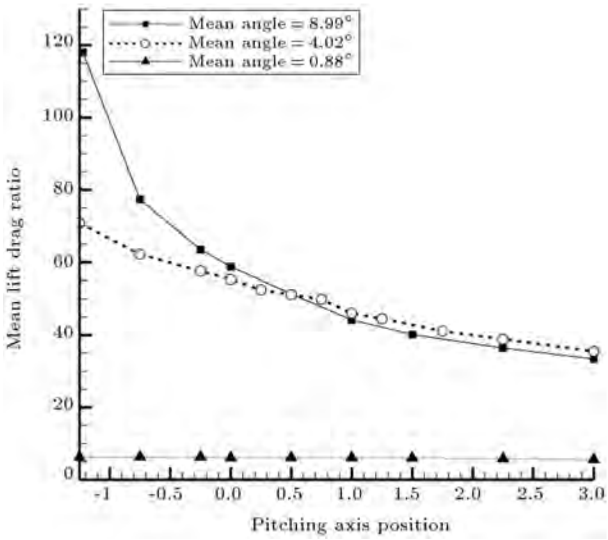

Figure 22. Effect of pitching axis position on average lift to drag ratio ($k = 0.133$, $\alpha_0 = 4°$).

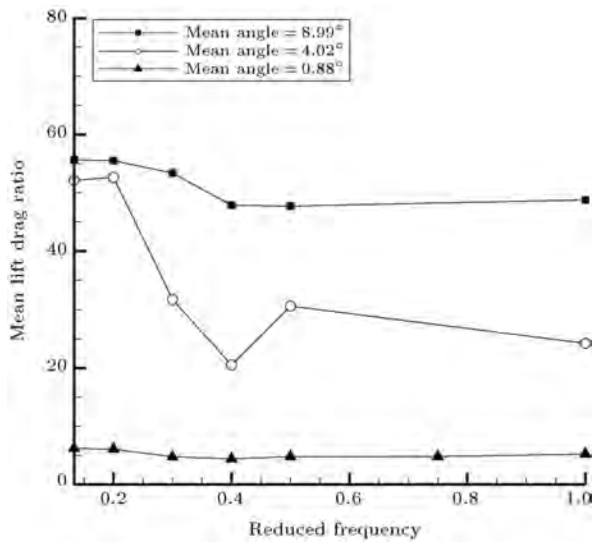

Figure 23. Effect of reduced frequency on average lift to drag ratio ($X_{cp} = 0.25$, $\alpha_0 = 4°$).

Figure 22 shows the effect of pitching axis position on average lift to drag ratio for $k = 0.133$, $\alpha_0 = 4°$. It is obvious that pitching axis position is not effective on average lift to drag ratio for $\alpha_m = 0.88°$. However, for higher mean angles, positive positions and distancing from the trailing edge lead to a reduction in average lift to drag ratio. Inversely, negative values and displacing from the leading edge in front of the airfoil bring about very high values of this ratio. Further, in negative positions, it can be observed that if mean angle of attack is selected at high value, average lift to drag ratio will become maximum.

It can be seen from Figure 23 that very low reduced frequencies (less than $k = 0.2$) result in high average lift to drag ratio for high mean angles. Thus, to maximize the ratio or to improve the flight efficiency in high Reynolds flows, it is required that a high mean angle of amplitude with a low reduced frequency is selected.

6. Conclusions

In this article, the unsteady flow around a pitching airfoil at high Reynolds number is investigated. Using the Coarse Grid CFD method, surface vorticity confinement and a multi zone adaptive grid, simultaneously, leads to a high-speed scheme that greatly reduces the required computational time, while the accuracy of the results is acceptable. Therefore, we have been able to explore the effects of different unsteady parameters on pitching airfoil aerodynamic coefficients.

According to the results, moving the pitching center location to the left or right sides has different consequences. Firstly, positive pitching axis positions or distancing from the trailing edge in back of the airfoil, results in enhancing the maximum and average lift and drag coefficients, while the minimum coefficient is not changed. Also, this reduces the average lift to drag ratio mainly at high mean angles. Thus, in some practical situations, in which only lift force is important, it is appropriate that the pitching center be placed in positive positions far from the trailing edge. Secondly, if the purpose is increasing the lift and simultaneously decreasing the drag, it is necessary that the pitching axis position be situated in front of the airfoil far from the leading edge. This also results in the increasing of average lift to drag ratio. Furthermore, the enlarging oscillation amplitude at high Reynolds flow, generally, has no considerable influence on the lift to drag ratio or efficiency of the flight. In addition, to maximize the average lift to drag ratio at high Reynolds flows, lower frequencies are desired. Finally, it should be stated that at lower mean angles of attack, unsteady parameters have no influence on the average lift coefficient.

References

1. McCroskey, W.J. "The phenomenon of dynamic stall", NASA report: NASA/TM-81264-1981.
2. Piziali, R.A. "An experimental investigation of 2D end 3D oscillating wing aerodynamics for a range of angle of attack including stall", NASA Technical Memorandum, No. 4632. Ames, CA:NASA 4632, Chalmers University of Technology (1993).
3. Tuncer, I., Wu, J. and Wang, C. "Theoretical and numerical studies of oscillating airfoils", *AIAA Journal*, **28**(9), pp. 1615-1624 (1990).
4. Akbari, M. and Price, S. "Simulation of dynamic stall for a naca 0012 airfoil using a vortex method", *Journal of Fluids and Structures*, **17**, pp. 855-874 (2003).
5. Sarkar, S. and Venkatraman, K. "Influence of pitching angle of incidence on the dynamic stall behavior of a symmetric airfoil", *European Journal of Mechanics B/Fluids*, **27**, pp. 219-238 (2008).
6. Martinat, G., Braza, M., Hoarau, Y. and Harran, G. "Turbulence modelling of the flow past a pitching NACA0012 airfoil at105 and 106 Reynolds numbers", *Journal of Fluids and Structures*, **24**, pp. 1294-1303 (2008).
7. Amiralaei, M.R., Alighanbari, H. and Hashemi, S.M. "An investigation into the effects of unsteady parameters on the aerodynamics of a low Reynolds number pitching airfoil", *Journal of Fluids and Structures*, **26**, pp. 979-993 (2010).
8. You D. and Bromby W. "Large-eddy simulation of unsteady separation over a pitching airfoil at high Reynolds number", *Seventh International Conference on Computational Fluid Dynamics (ICCFD7)*, Big Island, Hawaii, July 9-13 (2012).
9. Ou, K. and Jameson, A. "Optimization of flow past a moving deformable airfoil using spectral difference method", *41st AIAA Fluid Dynamics Conference and Exhibit*, 27-30 June 2011, Honolulu, Hawaii, AIAA 2011-3719 (2011).
10. Steinhoff, J. "Vorticity confinement: a new technique for computing vortex dominated flows", *Frontiers of Computational Fluid Dynamics*, D.A. Caughey and M.M. Hafez, Eds., J. Wiley & Sons (1994).
11. Hu, G., Grossman, B. and Steinhoff, J. "A numerical method for vortex confinement in compressible flow", AIAA-00-0281 (2000).
12. Lynn, N.F. and Steinhoff, J. "Large Reynolds number turbulence modeling with vorticity confinement", *18th AIAA Computational Fluid Dynamics Conference*, 25-28, Miami, FL June (2007).
13. Moulton, M. and Steinhoff, J. "A technique for the simulation of stall with coarse-grid CFD", AIAA-00-0277 (2000).
14. Wenren, Y., Fan, M., Dietz, W., Hu, G., Braun, C., Steinhoff, J. and Grossman, B. "Efficient Eulerian computation of realistic rotorcraft flows using vorticity confinement", AIAA-01-0996 (2001).
15. Dietz, W.E. "Application of vorticity confinement to compressible flow", *42nd AIAA Aerospace Sciences Meeting and Exhibit*, Reno, Nevada, 5-8 January (2004).
16. Butsuntorn, N., Jameson, A. "Time spectral method for rotorcraft flow with vorticity confinement", *26th AIAA Applied Aerodynamics Conference*, Honolulu, Hawaii, pp. 18-21 (2008).
17. Bagheri-Esfeh, H. and Malek-jafarian, M. "Development of artificial dissipation schemes and compressible vorticity confinement methods", *Journal of Aerospace Engineering*, **225**(8), pp. 929-945 (2011).
18. Nakahashi, k. and Deiwert, G.S. "Three dimensional adaptive grid method", *AIAA Journal*, **124**(6), pp. 948-954 (1999).
19. Murayama, M., Nakahashi, K. and Matsushima, K. "Unstructured dynamic mesh for large movement and deformation", *AIAA Conf.*, Paper 122 (2002).
20. Nadarajah, S.K. and Jameson, A. "Optimal control of unsteady flows using a time accurate method", *9th AIAA/ISSMO Symposium on Multidisciplinary Analysis and Optimization Conference*, Paper 5436 (2002).
21. Jameson, A., Schmidt, W. and Turkel, E. "Numerical solutions of the Euler equations by finite volume methods using runge-kutta time-stepping schemes", *AIAA Journal*, **81**, pp. 1259 (1981).
22. Spalart, P.R. and Allmaras, S.R. "A one equation turbulence model for aerodynamic flows", *AIAA 92-0439, AIAA 30th Aerospace Sciences Meeting and Exhibit* , Reno, NV, January (1992).

Biographies

Mahmoud Pasandideh Fard obtained a BS degree in Heat and Fluid Engineering, in 1985, an MS degree in Energy Conversion Engineering from Ferdowsi University of Mashhad, Iran, in 1988, and a PhD degree in Aerodynamics from Sydney University, Australia, in 1996. He is currently on the academic staff of Ferdowsi University of Mashhad, Iran. His research interests include supersonic and subsonic aerodynamics, hydrodynamics, cavitation and supercavitation, aerodynamics and hydrodynamics of projectiles and missiles, and turbulent boundary flow. He has completed several industrial projects and has presented and published more than 50 conference and 20 journal papers in his fields of interest.

Majid Malek-Jafarian was born in Mashhad, Iran, in 1975. He received a BS in Fluid Mechanics, an MS degree in Energy Conversion, in 1999, and a PhD degree, in 2006, all from the Mechanical Engineering Department of Ferdowsi University of Mashhad, Iran. His research interests include turbulence modeling, aerodynamics and optimization, and he is currently working in the Mechanical Engineering Department of the University of Birjand, Iran.

Ali Heydari was born in Mashhad, Iran, in 1983. He received a BS degree in Mechanics, in 2006, and an MS degree in Energy Conversion, in 2006, from the Mechanical Engineering Department of Ferdowsi University, Iran, where he is currently a PhD degree student in the same subject. His research interests include CFD, unsteady aerodynamics, boundary layer characteristics and solar energy, and he is currently working on the academic staff of the Mechanical Engineering Department at the Islamic Azad University of Semnan, Iran.